Influence of seawater exchanges across the Bab-el-Mandeb Strait on sedimentation in the Southern Red Sea during the last 60 ka

Alexandra Bouilloux, Jean-Pierre Valet, Franck Bassinot, Jean-Louis Joron, Fabien Dewilde, Marie-Madeleine Blanc-Valleron, Eva Moreno

PALEOCEANOGRAPHY, VOL. 28, 675–687, doi:10.1002/2013PA002544, 2013

Influence of seawater exchanges across the Bab-el-Mandeb Strait on sedimentation in the Southern Red Sea during the last 60 ka

Alexandra Bouilloux,[1] Jean-Pierre Valet,[1] Franck Bassinot,[2] Jean-Louis Joron,[1,3] Fabien Dewilde,[2] Marie-Madeleine Blanc-Valleron,[4] and Eva Moreno[4]

Received 1 August 2013; revised 8 October 2013; accepted 16 October 2013; published 3 December 2013.

[1] The location of core MD92-1008 close to the southern edge of the Red Sea is ideal to study the evolution of seawater exchanges with the Northern Indian Ocean through the Bab-el-Mandeb narrow strait. The present study was aimed at documenting the paleoceanographic evolution of this area over the past 60 ka using high-resolution magnetic, sedimentological, and geochemical indicators. Two modes of variability dominate the records: (i) long-term, glacial-interglacial variations and (ii) rapid, millennial scale variability (Dansgaard-Oeschger type) during the last glacial period. Changes in magnetic concentration were documented from natural and laboratory magnetizations after proper normalization. They are inversely correlated to the total organic carbon (TOC) content, pointing out the key role played by reductive dissolution of magnetite on the evolution of magnetic concentration. Based on the temporal evolution of TOC, $CaCO_3$, and planktonic $\delta^{13}C$, we suggest that past changes in the organic matter content (i) were closely linked to glacio-eustatic variations which modulated long-term seawater exchanges and nutrient supplies to the Red Sea through the narrow Bab-el-Mandeb Strait and (ii) reflect millennial-scale changes in productivity driven by monsoon wind intensity which controlled the amount of nutrient-rich intermediate waters upwelled in the Gulf of Aden during the summer season and advected into the Southern Red Sea. The sea level rise following the onset of deglaciation generated a rapid flush of detrital material that was accumulated on the continental margins and on the previously emerged zones of the Bab-el-Mandeb area.

Citation: Bouilloux, A., J.-P. Valet, F. Bassinot, J.-L. Joron, F. Dewilde, M.-M. Blanc-Valleron, and E. Moreno (2013), Influence of seawater exchanges across the Bab-el-Mandeb Strait on sedimentation in the Southern Red Sea during the last 60 ka, *Paleoceanography*, *28*, 675–687, doi:10.1002/2013PA002544.

1. Introduction

[2] The Red Sea is a long (1930 km) and narrow (230 km) marginal sea located in an arid environment. The terrigenous material found in marine sediments is predominantly eolian, originating from Northern Africa and/or from the Arabian peninsula [*Van Campo et al*., 1982; *Clemens and Prell*, 1990; *deMenocal*, 2004; *Kolla et al*., 1976; *Leuschner and Sirocko*, 2000; *Sirocko and Lange*, 1991; *Sirocko et al*., 1993, 2000]. The limited precipitations, below 100 mm/yr [*Grasshoff*, 1975; *Pedgley*, 1974], and the intense evaporation result in a net loss of ~2000 mm/yr [*Grasshoff*, 1975; *Morcos*, 1970; *Siedler*, 1969; *Sofianos et al*., 2002]. This loss is compensated by water inflow in the Southern Red Sea through the unique connection with the northern Indian Ocean, at the shallow Bab-el-Mandeb Strait (sill depth 137 m) [*Sheppard*, 2000].

[3] The water inflow through the Bab-el-Mandeb Strait is crucial to maintain the nutrient balance and pelagic primary productivity. The Red Sea is nutrient-limited and primary productivity is low compared to other oceans due to the deserts that surround this marginal sea (lack of major riverine inputs) and due to the water column stratification, which prevents the efficient recycling of nutrients to the euphotic zone. While nitrogen fixation seems to compensate partly for the loss of nitrates associated to the burial of organic matter, the deficit in phosphate appears to be only compensated by the lateral advection of nutrient-rich waters from the Gulf of Aden [*Naqvi et al*., 1986] which can be readily documented from the higher nutrient concentrations in the Southern Red

Additional supporting information may be found in the online version of this article.

[1]Institut de Physique du Globe de Paris, UMR 7154, CNRS, Université Paris Diderot, Sorbonne Paris-Cité, 1 rue Jussieu, FR-75238 Paris Cedex 05, Paris, France.
[2]Laboratoire des Sciences du Climat et de l'Environnement (CEA-CNRS-UVSQ), Domaine du CNRS, Avenue de la Terrasse, Gif-sur-Yvette, France.
[3]Sciences de la Terre, Laboratoire Pierre-Süe, CEA, Paris, France.
[4]Muséum National d'Histoire Naturelle, UMR 7207, Paris, France.

Corresponding author: J.-P. Valet, Institut de Physique du Globe de Paris, Université Paris Diderot, Sorbonne Paris-Cité, UMR 7154, CNRS, 1 rue Jussieu, FR-75238 Paris CEDEX 05, France. (valet@ipgp.fr)

0883-8305/13/10.1002/2013PA002544

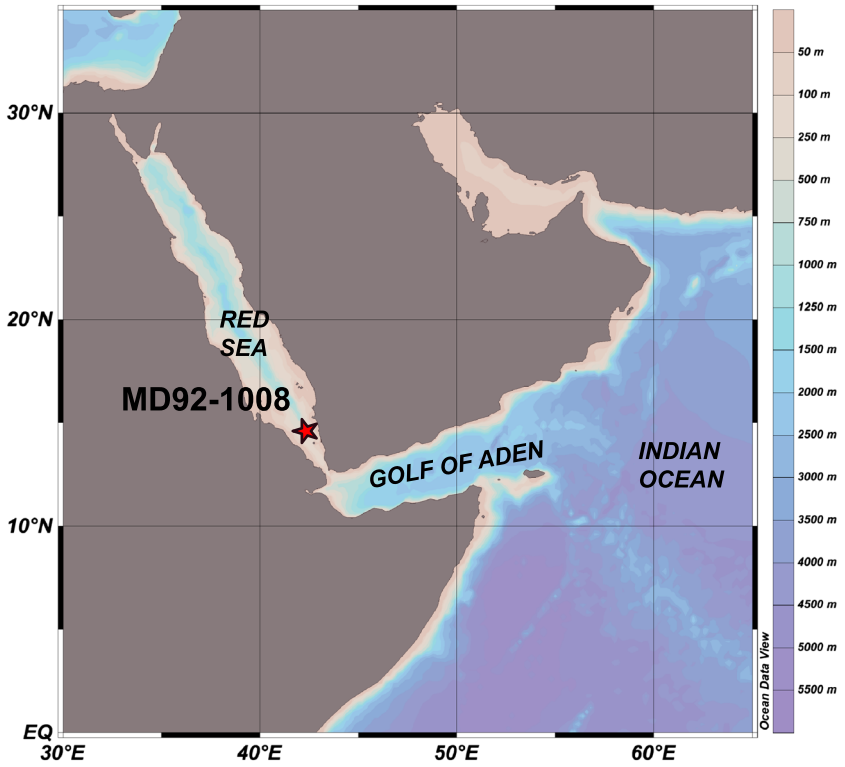

Figure 1. Bathymetric map modified from ODV4. 5. 1 (Schlitzer, R., Ocean Data View, http://odv.awi.de, 2011) showing the geographic position of core MD92-1008 in the Southern Red Sea.

Sea [*Naqvi et al*., 1986; *Poisson et al*., 1984]. The combination of primary productivity boosted by this nutrient supply [*Weikert*, 1987] and vertical stratification induce the development of a strong oxygen minimum zone, with oxygen concentration around 0.5 ml/L at approximately 300–400 m near the Bab-el-Mandeb area [*Neumann and McGill*, 1962; *Fenton et al*., 2000].

[4] Today, water exchanges across the Bab-el-Mandeb Strait and nutrient supply are modulated on a seasonal timescale by monsoon wind reversal. The balance of deep water outflow and surface water inflow characterizes the winter regime, lasting globally from November to early June. From June to October, southwest monsoon winds drive a strong Ekman pumping along the western coasts of the northern Arabian Sea and the Gulf of Aden, resulting in intense upwellings and an increase of primary productivity [*Bassinot et al*., 2011; *Lévy et al*., 2007; *Sharma*, 1978; *Shetye et al*., 1990]. The upwelled, nutrient-rich water raised at intermediate depths in the Gulf of Aden is gradually forced toward the Red Sea, through the Bab-el-Mandeb Strait [*Naqvi et al*., 1986; *Siddall et al*., 2004; *Smeed*, 1997; *Sofianos et al*., 2002].

[5] At glacial-interglacial timescales, it has been suggested that water exchanges varied in response to sea level changes, being reduced during glacial periods when the sill depth at the Bab-el-Mandeb Strait was reduced to ~17 m [*Rohling et al*., 2007; *Siddall et al*., 2003, 2004; *Sirocko*, 2003]. The impact of glacio-eustatism on the Red Sea outflow was recently documented by *Malaizé et al*. [2009] who showed that in the Socotran area, episodes of sea level rise during the penultimate deglaciation were associated with plumes of warm and salty water from the Red Sea. Little is known, however, about impacts of water exchanges on the sedimentation in the Southern Red Sea and, in particular, about the potential impact of sea level changes, insolation forcing, or high-latitude millennial-scale variability on the sedimentation, and pelagic productivity. In order to unravel these potential effects, we studied core MD92-1008 (14°25′86″N; 42°13′62″E) located only ~230 km to the north of the Bab-el-Mandeb Strait, at 708 m of water depth (Figure 1). This ~17 m long piston core has provided a continuous planktonic $\delta^{18}O$ record (*Globigerinoides ruber*), covering the last 60 ka (average sedimentation rate of ~30 cm/ka).

2. Stable Isotopic Stratigraphy and ^{14}C Dating

[6] The sediment retrieved in core MD92-1008 is a hemipelagic, clay-rich ooze with abundant foraminifers. The sedimentary series does not present apparent turbiditic or reworked layers. We sampled the core using U channels for continuous magnetic measurements and with plastic cubes taken at ~5 to 10 cm interval for detailed geochemical, mineralogical, and magnetic analyses. We measured the oxygen (and carbon) isotopic composition of the planktonic foraminifera *Globigerinoides ruber* (white, sensu stricto) on a Finnigan DeltaPlus mass spectrometer at the Laboratoire des Sciences du Climat et de l'Environnement (LSCE) on 336 samples taken every 5 cm. The mean sample size is 5–10 shells of *G. ruber* picked in the narrow 250–315 µm size fraction. Expressed in ‰ is $\delta^{18}O$ versus Vienna Peedee belemnite, with respect to NBS19 calcite standard [*Coplen*, 1988]. The mean external reproducibility (1σ) estimated from multiple analyses of a LSCE carbonate standard is ± 0.05‰.

Table 1. AMS ^{14}C Ages for Core MD92-1008 From the Southern Red Sea

Sample Code	Sampling Depth (cm)	Radiocarbon Laboratory	Sample	AMS ^{14}C Age (^{14}C yr B.P.)	Calibrated Age (calendar yr B.P.)
MD92-1008/ I-25.5 cm	25.5	Poznan Radiocarbon Laboratory	Poz-18569	1,335 ± 30	728 ± 160
MD92-1008/ I-33.5 cm[a]	33.5	Laboratoire de Mesures Carbone 14 UMS 2572	SacA 22734	1,540 ± 40	965 ± 168
MD92-1008/ I-84 cm	84	Poznan Radiocarbon Laboratory	Poz-21477	2,535 ± 30	2,003 ± 160
MD92-1008/ II-27 cm	165	Poznan Radiocarbon Laboratory	Poz-21474	4,240 ± 40	4,119 ± 168
MD92-1008/ II-111.5 cm	249.5	Poznan Radiocarbon Laboratory	Poz-21476	6,870 ± 40	7,236 ± 168
MD92-1008/ II-146.5 cm	284.5	Poznan Radiocarbon Laboratory	Poz-21478	8,360 ± 50	8,718 ± 179
MD92-1008/ III-33.5 cm[a]	321.5	Laboratoire de Mesures Carbone 14 UMS 2572	SacA 22735	9,415 ± 50	10,053 ± 179
MD92-1008/ IV-10 cm	448	Laboratoire de Mesures Carbone 14 UMS 2572	SacA 25095	12,280 ± 60	13,565 ± 191
MD92-1008/ IV-94 cm	532	Laboratoire de Mesures Carbone 14 UMS 2572	SacA 25096	13,570 ± 70	15,673 ± 204
MD92-1008/ V-44.5 cm	632.5	Laboratoire de Mesures Carbone 14 UMS 2572	SacA 25097	17,780 ± 90	20,442 ± 233
MD92-1008/ V-69.5 cm[a]	657.5	Laboratoire de Mesures Carbone 14 UMS 2572	SacA 22736	21,190 ± 100	24,629 ± 249
MD92-1008/ VII-40.5 cm	928.5	Laboratoire de Mesures Carbone 14 UMS 2572	SacA 25098	30,780 ± 250	34,815 ± 521
MD92-1008/ VII-79.5 cm	967.5	Laboratoire de Mesures Carbone 14 UMS 2572	SacA 24010	33,210 ± 250	37,162 ± 521

[a]AMS^{14}C on mixing *G. ruber* white and *G. sacculifer*, for other samples only on *G. ruber* white. Calibrated ages are indicated with 2σ error.

[7] Thirteen ^{14}C ages were obtained by accelerator mass spectrometry (AMS) at the laboratoire de mesure du carbone 14 (Saclay, France) and at the Poznan Radiocarbon Laboratory (Poland) on calcite shells of *G. ruber* and *Globigerinoides sacculifer* planktonic foraminifera (Table 1). These AMS^{14}C ages were converted to calendar ages with the CALIB6.O software [*Stuiver and Reimer*, 1993], using the 2009 marine calibration curve [*Reimer et al*., 2009] and assuming a global surface reservoir age of 400 years with a regional correction of $\Delta r = 163$ yr ± 74 yr [*Southon et al*., 2002]. The reservoir age correction (Δr between 100 and 180 years) is in agreement with those previously used to construct timescales of Red Sea cores [*Arz et al*., 2003a, 2003b, 2006, 2007; *Legge et al*., 2006, 2008; *Trommer et al*., 2010]. The age model of core MD92-1008 was completed beyond ~40 ka B.P. by tuning graphically the oxygen isotope record to the reference LR04 curve [*Lisiecki and Raymo*, 2005] using the AnalySeries 2.0.4.2 software [*Paillard et al*., 1996]. The age model was established by linear interpolation, assuming a constant deposition rate between two adjacent tie points (supporting information Figure S1).

[8] Results indicate that core MD92-1008 covers the past 60 ka B.P. (Figure 2a) and that the ~5 cm sampling resolution of the δ^{18}O record corresponds to an average temporal resolution of ~200 years. The marine isotopic stages (MIS) 1 to 4 [*Emiliani*, 1955; *Prell et al*., 1980] are clearly identified. The mean deposition rate is ~30 cm/ka. The age model shows a striking low centered at 25 ka B.P., between the ^{14}C dated samples at 657.50 m (24.63 ka B.P.) and 928.5 m (34.52 ka B.P.), respectively. This low may either correspond to a

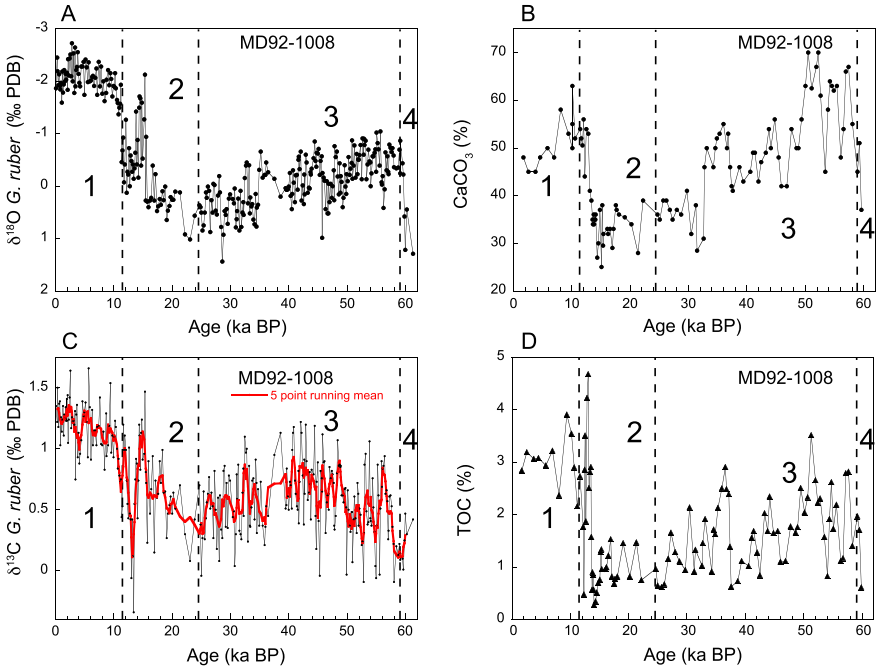

Figure 2. Geochemical parameters measured in core MD92-1008 for the past 62 ka. (a) Oxygen isotope stratigraphy derived from the δ^{18}O variations recorded by *G. ruber* foraminifera. Numbers refer to the isotope stages of *Emiliani* [1955]. (b) Carbonate content and (c) δ^{13}C. (d) Total organic carbon content.

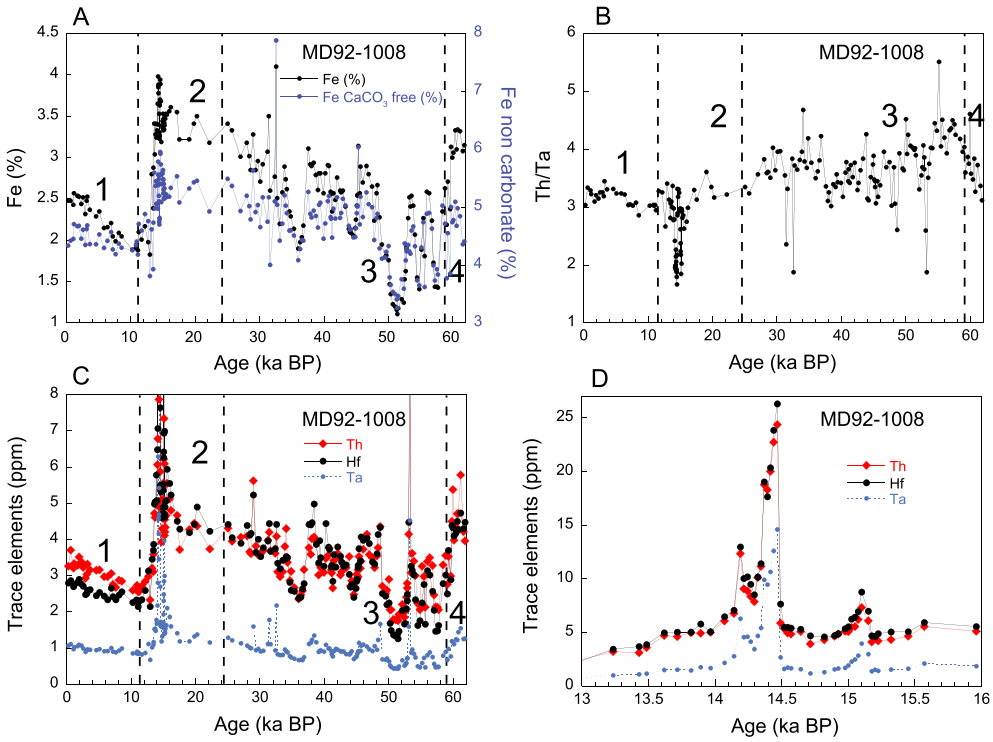

Figure 3. (a) Concentration of major and trace elements. Fe is plotted before and after correction for $CaCO_3$. (b) Th/Ta ratio. (c) Th, Hf, and Ta showing two periods of strong input, (d) close-up of the 13–16 ka B.P. time period characterized by a large excursion in Th, Hf, and Ta.

drastic reduction of sedimentation or suggest the presence of a small hiatus within this interval, which would be improperly resolved by the dating resolution. Under visual inspection, however, the sediment does not show any evidence of an abrupt change in sedimentation that could point out a hiatus.

[9] Carbon dating limitations result from analytical uncertainties and from uncertainties associated with the conversion to calendar ages. In addition, one should not forget that past variations in water exchange through the Bab-el-Mandeb Strait have likely affected the water residence time in the Red Sea and, therefore, the age reservoir [*Biton et al.*, 2008; *Rohling and Zachariasse*, 1996; *Rohling et al.*, 1998; *Siddall et al.*, 2003, 2004]. For the lower part of the record, it is usually admitted that graphical correlation and astronomical tuning can lead to uncertainties in the range of ± 5 ka [*Martinson et al.*, 1987].

3. Chemical Analyses

3.1. Carbonates

[10] The total carbonate content (in weight %) of 110 samples was determined from the pressure of CO_2 released through the reaction of 100 mg of dry, grounded sediment with 0.4 cm^3 of HCl 8N (absolute error ~1%). We estimated the wet and dry bulk densities of samples of known volume by measuring their wet and dry (after 48 h at 50°C) weights. The carbonate content ranges from 25% to 70%. A low value (~35%) is found during MIS 4, whereas the onset of MIS 3 is characterized by high values (60%) and by large fluctuations (± 10%–15%, Figure 2b). The percent of $CaCO_3$ decreases during MIS 3 and MIS 2, reaching its minimum of ~25% at about 15 ka B.P. This low is followed by an abrupt increase in less than a couple of thousand years. Values reach almost 55% at about 12 ka B.P. and in the early Holocene. Then the amount of $CaCO_3$ steadily decreases upward, without secondary fluctuations superimposed on this general trend.

[11] The density profile does not show any increasing trend with depth as it would be expected from burial compaction (Figure S2). The density and carbonate profiles are opposite to each other. This inverse relationship may be explained by the fact that $CaCO_3$-rich intervals contain a higher proportion of foraminifera shells and thus large intra-particle porosity (inside chambers) that reduces the sample density. The anticorrelation of these two parameters is also apparent in the short scale-variability, particularly during MIS 3.

3.2. $\delta^{13}C$ and Total Organic Carbon (TOC)

[12] The $\delta^{13}C$ analyses were performed on a DeltaPlus Mass spectrometer at LSCE (see above) with a mean external reproducibility of ± 0.03‰ (1σ). The $\delta^{13}C$ record of the surface-dwelling planktonic *G. ruber* indicates rapid oscillations superimposed on a long-term, glacial-interglacial change (Figure 2c). Millennial-scale variations of high amplitude (≥ 0.5‰) seem to characterize MIS 3, but the $\delta^{13}C$ record is difficult to interpret because of high scattering. In order to extract more statistically robust oscillations, we performed a five-point window moving average. The smoothed signal enhances the visibility of the millennial-scale variations, resulting, for instance, in the three relatively distinct periods of $\delta^{13}C$ minima at ~36, 50, and 60 ka B.P. The $\delta^{13}C$ values drop between MIS 2 and MIS 1 with low $\delta^{13}C$ levels centered on ~13.4 ka B.P.

[13] Total organic content (%) has been measured on 110 samples using a LECO IR 212 elemental combustion analyzer (precision ~0.02%) at the Institut des Sciences de la Terre de Paris (ISTeP, Université Pierre et Marie Curie, Paris). The $CaCO_3$ content was independently obtained by gas volumetric analysis on an aliquot of each sample (see above) and the TOC was estimated by subtracting this mineral carbon from the LECO total carbon content.

[14] High TOC contents range between 0.2% and ~4.7% (mean value of ~2%) (Figure 2d). A progressive decrease takes place during MIS 3 to MIS 2, with mean values dropping from ~3% to 0.2%. On this progressive trend are superimposed several large amplitude (up to ± 2%) oscillations. During the transition from MIS 2 to MIS 1, the TOC reaches peak values as high as 4.7%.

3.3. Elemental Composition of Sedimentary Material

[15] We scrutinized the relative contribution of major (e.g., Al and Fe) and trace (e.g., Th, Ta, and Hf) elements on 202 bulk samples through neutron activation analyses at the Pierre Sue Laboratory (CEA, Saclay). We applied the technique described in *Joron et al*. [1997]. Here, we focus on four elements: iron (Fe), key component as far as magnetic properties are concerned; and Thorium (Th); Tantalum (Ta); and Hafnium (Hf), which were successfully used to differentiate the sediment sources in sediments from the Northern Indian Ocean [*Bouilloux et al*., 2013].

[16] High Fe values (~3%) are measured in MIS 4 (bottom interval). Iron content drops down to ~1.2% at ~50 ka, and then shows a progressive upward increase during MIS 3 and MIS 2, reaching maximal values (up to ~4%) at ~14 ka B.P. (Figure 3a). This sharp and narrow Fe concentration is also reproduced by the Th/Ta ratio (Figure 3b). After this peak, the %Fe drops rather abruptly by more than 2% in less than ~2 ka, reaching values of ~1.2% at about 12 ka B.P. The Fe content remains low during the Holocene, but with an increasing trend upward. Large amplitude changes are superimposed on these long-term trends. Two of the three peaks present in the TOC and $\delta^{13}C$ records at ~36, 50 ka B.P. are also characterized by low Fe contents.

[17] It is striking that Fe concentration changes (Figure 3a) almost mimic those of $\%CaCO_3$ (Figure 2b), with opposite long-term trends (R^2 of ~0.87) as well as anticorrelated shorter variations within MIS 3-MIS 2 and over the 14–12 ka B.P. interval. After correction for carbonate dilution, iron fluctuations are significantly smoothed out (Figure 3a), especially over the 16–30 ka B.P. interval and the Holocene. Yet, major structures are still present and short-term, large amplitude fluctuations in MIS 3 were not altered by the correction.

[18] Down-core variations of Th, Hf, and Ta are all characterized by two periods of high values at ~15 and 54 ka B.P., with a major change at ~15 ka B.P. (Figure 3c). A global increase of those three elements characterizes the whole MIS 3-MIS 2. The enlarged view of the 13–16 ka B.P. interval shows that this event is characterized by three excursions in the Th, Hf, and Ta concentrations (Figure 3d).

4. Magnetic Study

4.1. Paleomagnetic Directions

[19] The natural remanent magnetization (NRM) of the U channels was stepwise demagnetized every 10 milliTesla (mT) up to 100 mT down to 16.5 m. Measurements were performed at 2 cm intervals with a 2-G pass-through magnetometer in the shielded room of the Institut de Physique du Globe de Paris (IPGP) following the protocol of *Nagy and Valet* [1993]. Complete demagnetization was usually attained at 60 mT. Characteristic remanent magnetization (ChRM) directions were isolated by fitting straight lines through the data and the origin of the demagnetization diagrams using the Paleomac 6.2 software [*Cogné*, 2003] (Figure S3a). A few samples strongly resistant to alternating field (AF) demagnetization did not yield any suitable characteristic component. ChRM declinations and inclinations are plotted as a function of age in Figures S3b and S3c. In the absence of orientation within the horizontal plane, the mean declination value for the entire core was set to zero. The inclination depicts a succession of oscillations of about 20° in amplitude. The mean inclination of 31.5° is 4.5° higher than the inclination of the geocentric axial dipole at the site latitude.

4.2. Magnetic Concentration

[20] Low-field susceptibility (K) was measured every 2 cm at the surface of the sediment using a Bartington susceptibility meter coupled to a MS2E sensor at the Muséum National d'Histoire Naturelle (MNHN) of Paris. The susceptibility increases from 60 to 11 Ka B.P. (1400 to 470 cm) and then abruptly drops to values as low as 4×10^{-5} SI for the past 10 ka B.P. (which correspond to the upper 4 m of sediment) (Figure 4a). The density profile (see section 3.2) was used to convert the original K values into equivalent values of mass susceptibility (χ). We investigated whether the signal was heavily constrained by carbonate dilution, as somehow suggested by low values of carbonate opposed to high K during the deglaciation (Figures 2a and 4a). However, the amplitude of $CaCO_3$ fluctuations being much lower than for K, the carbonate-free mass susceptibility exhibits the same trend as the original signal (Figure 4b). The high K values (~24×10^{-5} SI) between ~14 and ~16 ka B.P. (540 and 470 cm) are divided in three short episodes. They culminate by a large and rapid decrease over a ~1.5 ka period. Low and stable values characterize the Holocene period.

[21] The strong susceptibility values in the 15.5–13.7 ka interval also coincide with strong NRM intensities (Figure S3d). The evolution of NRM_{20mT} (NRM demagnetized at 20 mT) shows a gradual increase between 32 and 14 ka B.P., followed by a large and sudden drop. Measurements of anhysteretic remanent magnetization (ARM) were performed (every 2 cm) in a 30 μT steady field and a 100 mT alternating peak field. The ARM_{20mT} profile is similar to that of NRM_{20mT} (Figures S3d and S3e) but with much larger amplitudes.

[22] The absence of erosional features at the bottom of this layer and the internal coherence of magnetic directions are not consistent with a turbiditic event. The Th/Ta and Ta/Hf ratios are compatible with a highly differentiated source of material. Particles in provenance of nearby volcanic areas are plausible candidates. Nevertheless, no shard glass was detected from microscopic examinations, which also suggests reworking of older volcanic material.

[23] The K and Fe down-core profiles display in-phase variations (Figures 3a, 4a, and 4b), but in contrast to K, a significant part of Fe is modulated by carbonate dilution. We infer that a large part of the Fe signal is linked to detrital components that do not have any significant effect on the

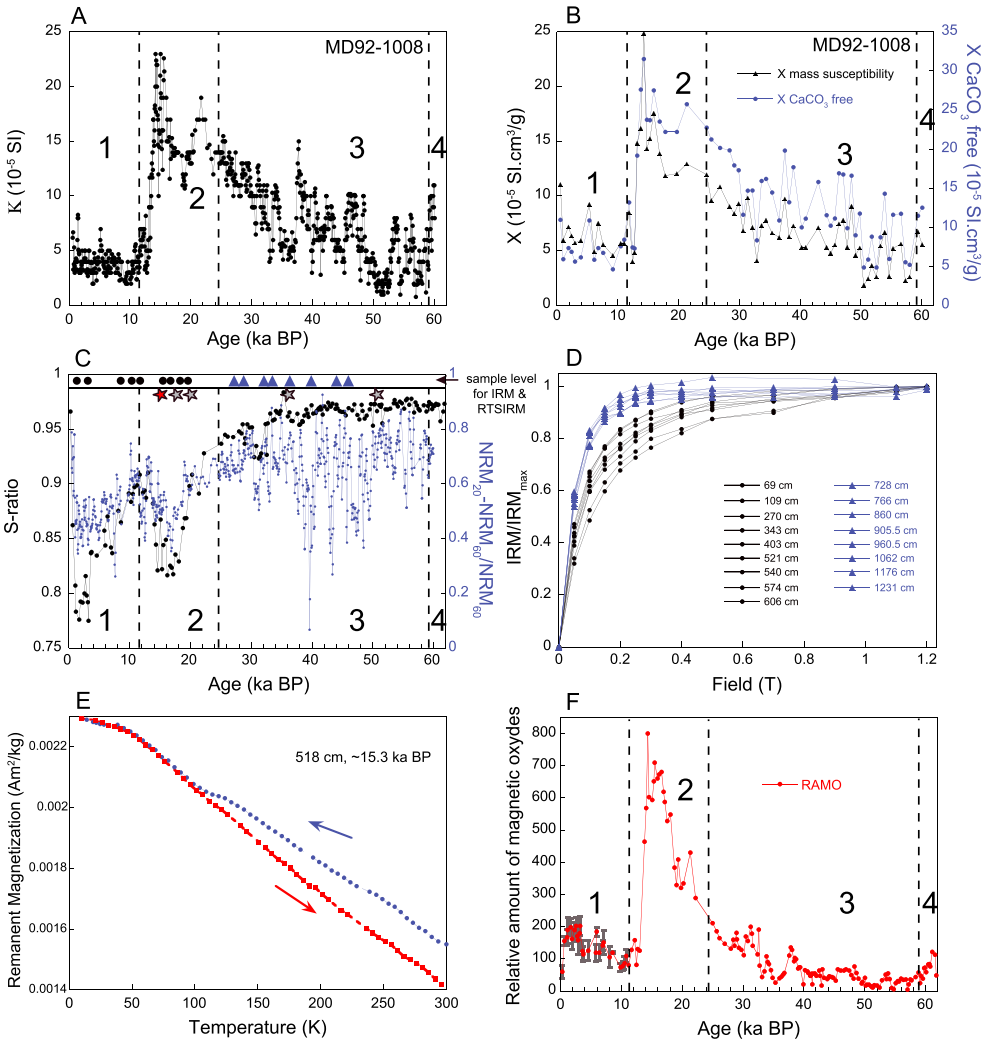

Figure 4. (a) Magnetic susceptibility and (b) mass susceptibility and $CaCO_3$ profiles of core MD92-1008 as a function of time. (c) Variations of the S ratio for core MD92-1008 and evolution of the R ratio (NRM_{20mT}-NRM_{60mT})/NRM_{60mT}). (d) IRM acquisition curves pointing out the existence of two distinct mineralogical families. (e) RT-SIRM cycle for one sample indicated by a red star in Figure 4c. The location of the other samples used for the same experiment is shown by gray stars. (f) Evolution of the relative amount of magnetic oxides (RAMO).

susceptibility. This implies that magnetic concentration indicators are not primarily driven by their respective amount within the detrital fraction, and that the magnetic mineralogy might play a significant role.

4.3. Magnetic Mineralogy

[24] An isothermal remanent magnetization (IRM) was imparted on 169 discrete samples in a direct field of 1 T and subsequently in a reverse field of 0.3 T to calculate the S ratio [*Bloemendal et al.*, 1992]. Surprisingly, we found out that (i) the levels with strong susceptibility were associated with higher coercivity minerals and that (ii) the levels between 60 and 30 ka B.P., which show S ratios close to one typical of low coercivity minerals (usually magnetite), were associated with low susceptibilities (Figure 4c).

[25] Experiments of stepwise acquisition of IRM were conducted on 17 cubes taken within and outside the K peak (Figure 4d). Significant differences between the saturation isothermal remanent magnetization (SIRM) acquisition curves are obvious from the plot in Figure 4c and fully consistent with the S ratio evolution. The evolution of the (NRM_{20}-NRM_{60})/NRM_{60} ratio (referred as the R ratio), which gives the amount of magnetization lost after demagnetization at 60 mT, and is indicative of its resistance to AF demagnetization presents a decrease from 0.7 to 0.4 at the top of the core (Figure 4c). This trend is opposite to the increase in magnetic intensity over the same interval and therefore confirms that a larger proportion of high coercivity minerals are accompanied by larger susceptibility values.

[26] In order to characterize the high coercivity component, room temperature-saturation isothermal remanent magnetization (RT-SIRM) experiments were performed on five samples with different susceptibility values. Measurements were conducted with the Quantum Design XL5 EverCool magnetic properties measurement system at IPGP after applying a 1 T field. Changes in magnetization during cooling

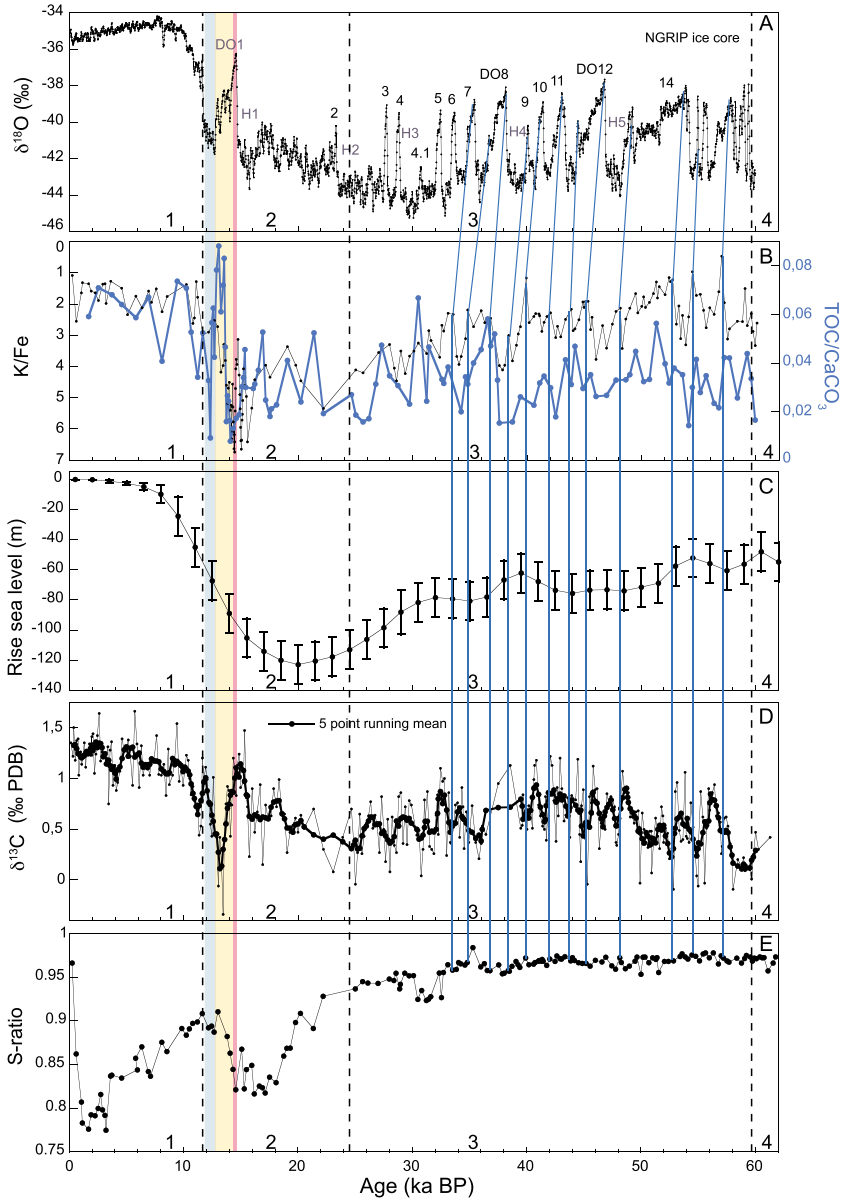

Figure 5. (a) $\delta^{18}O$ variations recorded in the NGRIP ice core using the GICC05 scale [*North Greenland Ice Core Project members*, 2004; *Andersen et al*., 2006] with the Dansgaard-Oeschger (DO) and Heinrich events and the intervals of the Younger Dryas (blue) and Bølling-Allerød (yellow). (b) Evolution of the K/Fe and TOC/$CaCO_3$ ratios. (c) Sea level estimates derived from *Waelbroeck et al*. [2002]. The purple band indicates the large excursion in Th at around 14.5 ka B.P. (Figure 3c). (d) Evolution of $\delta^{13}C$ (e) S ratio profile.

and heating were monitored by 5 K increments (300–10 and 10–300 K). The five cooling curves are characterized by a steep increase of the SIRM, which is typical of goethite (Figure 4e) [*Aubourg and Pozzi*, 2010; *Franke et al*., 2007; *Maher et al*., 2004]. The cooling and heating curves also exhibit a nonreversible Verwey transition at ~120 K.

[27] The presence of hematite should be indicated by the T ratio [*Meynadier et al*., 1992, 1995] which is the remaining percentage of IRM after heating to 600°C and is calculated as $(IRM\text{-}IRM_{600°C})/IRM_{600°C}$. We found no significant magnetization beyond 600°C and therefore no evidence of hematite. It could be argued that hematite disappeared due to mineralogical transformations of the sediment while heating up to 600°C. However, heating was performed in air so that most magnetic materials should have oxidized. We infer that magnetite is present over the entire core but there is a progressive increase of high coercivity material, most likely goethite, which culminates within the level of high K.

[28] Changes in the relative amount of magnetic oxides (RAMO) can be estimated by simulating a situation in which all magnetic grains would have the same magnetic mineralogy. This approach rests upon the conversion of the magnetization carried by high coercivity material (goethite/hematite) into the equivalent magnetization which would be carried by

the same amount of magnetite [*Bouilloux et al*., 2013]. This was achieved by taking into account the relative amount of high- versus low-coercivity material derived from the S ratio and the fact that the magnetization of magnetite is 200 times stronger than that of goethite [*O'Reilly*, 1984]. The correcting factor derived from this calculation is $C = 100.5 - (99.5 \times S)$, where S is the S ratio. It was applied to the values of magnetic susceptibility to provide the RAMO. In order to minimize uncertainties in these estimates, we averaged the values of three successive data points and referred to their standard deviation. The RAMO profile derived from 169 levels displays a very different picture than the initial susceptibility record (Figure 4f). The previous gradual increase from 60 to 14 ka B.P. has almost disappeared and the unique noticeable remaining feature is a large peak between 12–20 ka B.P. with the same amplitude (roughly a factor 4) as in the initial susceptibility but restrained to the end of MIS 2. It is generated by high coercivity material and thus reflects a large amount of goethite.

[29] Due to the large change of the magnetic mineralogy, any experiment aimed at describing the grain size variations was unlikely to yield results, because these experiments rely on the presence of a unique mineral.

5. Discussion

5.1. Eustatic and Climatic Imprints in the Southern Red Sea Sedimentation

[30] A dominant feature emerging from our results is that almost all parameters (i.e., TOC, Th, and K) display long-term oscillations (Figures 2–4), which resemble the $\delta^{18}O$ variations and suggest a strong climatic imprint. Because the $\%CaCO_3$ record shows high-amplitude fluctuations, dilution may explain a significant part of the variability shared between several proxies. In order to compensate for this potential dilution effect and extract their intrinsic signature, we relied on ratios (i.e., K/Fe, Th/Ta, and $TOC/CaCO_3$) to scrutinize the evolution of magnetic concentration, trace elements, and TOC. These indicators—together with the S ratio and the $\delta^{13}C$ records—are compared in Figure 5 to sea level fluctuations and to the North Greenland Ice Core Project (NGRIP) oxygen record. The boundaries of the marine isotopic stages have been indicated in each plot.

[31] A long-term influence of sea level fluctuations on the Southern Red Sea sedimentation is suggested by the overall resemblance between TOC and K records, on the one hand, and the *Waelbroeck et al*. [2002] glacio-eustatic sea level reconstruction, on the other hand (Figure 5c). The covariance between these records is particularly striking across the last glacial termination. At shorter (orbital) timescale, however, visual inspection or spectral analyses have failed to extract a clear signature of Earth's orbital precession in the MD92-1008 proxy records. This appears somewhat surprising considering the importance of low-latitude insolation changes in driving major intertropical climatic features such as the monsoons. Precession oscillations are clearly recorded, for instance, in the nearby Gulf of Oman [*Burns et al*., 1998], from the Arabian Sea [*Caley et al*., 2011; *Clemens and Prell*, 1990; *Clemens et al*., 1996; *Sirocko et al*., 1993] and from the Red Sea [*Hemleben et al*., 1996]. Two elements may explain the absence of a clear precession imprint in core MD92-1008: (1) the fact that over the last 60 ka covered by our short sedimentary record, two of the three precession cycles have a very low amplitude owing to the small eccentricity of the Earth's orbit and (2) the possibility that orbital-related variability is masked somewhat by shorter-scale changes (millennial).

[32] Millennial-scale changes are clearly observed on records from core MD92-1008. Several studies have already documented the remote impact of high-latitude, glacial rapid climatic variability on tropical areas and in particular on monsoon dynamics [e.g., *Arz et al*., 2007; *Leuschner and Sirocko*, 2000]. Within the limits of our age model, it is striking that almost each major feature of the K/Fe record can be correlated to the Dansgaard-Oeschger stadial-interstadial oscillations, clearly suggesting the impact of Northern Hemisphere millennial-scale variability on the sedimentation of the Southern Red Sea during MIS 3.

5.2. Early Diagenesis and Redox Conditions Control the Susceptibility Evolution

[33] The most striking feature is that the $TOC/CaCO_3$ profile is negatively correlated with the magnetic susceptibility normalized with respect to Fe (i.e., dilution-corrected, Figure 5). This relationship suggests that preservation of magnetite is inversely related to the TOC, an observation that has been frequently reported [*Abrajevitch and Kodama*, 2011; *Froelich et al*., 1979; *Karlin and Levi*, 1983; *Kawamura et al*., 2007; *Leslie et al*., 1990; *Liu et al*., 2004; *Richter et al*., 1999; *Roberts and Turner*, 1993; *Robinson et al*., 2000; *Rowan et al*., 2009]. High TOC values associated with low K levels reflect, therefore, diagenetic dissolution of magnetite while low TOC and high susceptibilities indicate very low iron reduction [*Snowball*, 1993]. In contrast to what has been observed in the Gulf of Aden [*Bouilloux et al*., 2013], the absence of correlation between K and the S ratio indicates that the iron released after dissolution of fine magnetite grains was not remobilized in the formation of high coercivity material. In the present case, the dependence between TOC and K is not only observed over long periods but also over short timescales, specifically remarkable during MIS 3 (Figure 5). This stresses the importance of understanding what drives millennial-scale TOC fluctuations in the Southern Red Sea.

5.3. Long-Term Control on TOC Variations in the Southern Red Sea: Sea Level Fluctuations and Water Exchanges Through the Bab-el-Mandeb Strait

[34] Despite being located at shallow water depth, close to landmass, limited detrital supply was brought to the site owing to the aridity of the surrounding continental areas, with weak riverine supplies and dominant airborne-transported particles. The high abundance of foraminifer shells and calcareous nannofossils and the positive correlation between the $CaCO_3\%$ and the $TOC/CaCO_3$ ratio clearly suggest that organic carbon found in the Southern Red Sea is predominantly of marine origin and that past changes in primary productivity likely explain much of the common variability between carbonate and carbon contents. This covariance is strong at millennial timescales but the $CaCO_3$ record displays, nevertheless, a somewhat steeper decrease across the glacial period and less variability across the last glacial termination than the TOC record (Figures 2b and 2d). Both these differences can result from the fact that: (i) pelagic primary

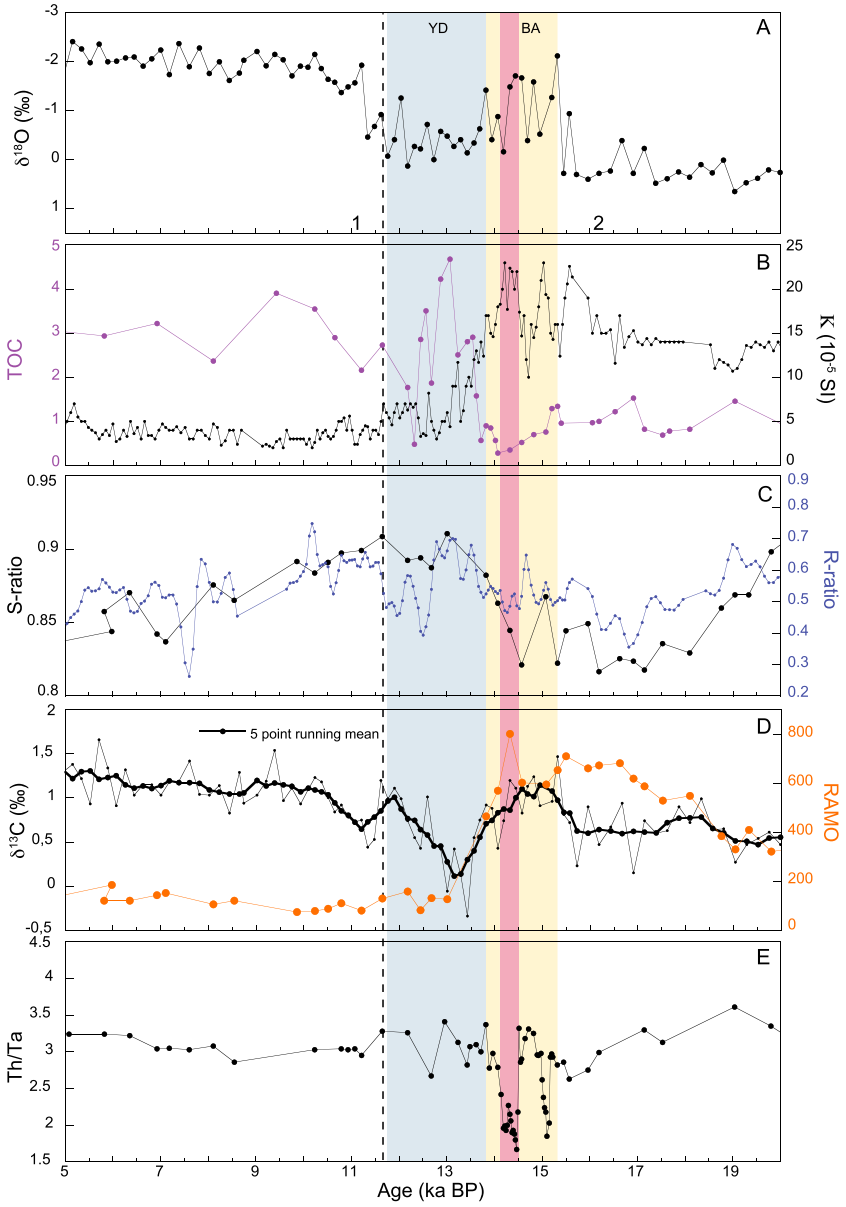

Figure 6. Magnetic, mineralogical, and geochemical indicators as a function of time during the 5–20 ka B.P. interval. (a) $\delta^{18}O$ of *G. ruber*, (b) Total organic carbon and magnetic susceptibility, (c) R and S ratios, and (d) RAMO and $\delta^{13}C$. (e) Th/Ta ratio.

productivity is not restricted to planktonic organisms producing carbonate shells and (ii) burial flux of TOC may also depend upon preservation changes. We have no data in the present study that would make it possible to estimate the importance of deep ventilation on the TOC content. Further work is in progress to address this issue through the use of proxies such as benthic ^{13}C and bulk ^{15}N.

[35] As seen above, the Red Sea is nutrient-limited and primary productivity is low compared to other oceans. Nutrient limitation is readily explained by the fact that deserts surround the Red Sea and that its stratification further prevents active recycling of nutrients to the surface from deeper waters. Nutrient balance and primary productivity today are ultimately linked, therefore, to the inflow of nutrient-rich waters from the Gulf of Aden through the Bab-el-Mandeb Strait [*Naqvi et al.*, 1986; *Poisson et al.*, 1984]. It has been suggested that exchanges of water varied at glacial-interglacial timescales, with smaller exchanges during glacial periods when the sill depth at the Bab-el-Mandeb Strait was reduced to ~17 m [*Rohling et al.*, 2007; *Siddall et al.*, 2003, 2004; *Sirocko*, 2003]. The strong resemblance between long-term changes in core MD92-1008 TOC record and the glacio-eustatic sea level reconstruction (Figure 5) suggests that, at glacial-interglacial timescales, primary productivity in the Southern Red Sea was strongly dependent upon the modulation of water exchanges through the Bab-el-Mandeb Strait, which controlled the amount of nutrients imported from the nearby Gulf of Aden. One cannot reject the possibility that changes in vertical nutrient recycling may have also played a role in the observed TOC variations. However, in the absence of indicators that could help us decipher between vertical and lateral advection of nutrients in the past, we make the

hypothesis that stratification always limits vertical mixing, particularly at times of low sea level when exchanges with the Gulf of Aden were more limited, resulting in the overall higher salinity of the Red Sea and a presumably stronger stratification at its southern end.

5.4. Millennial-Scale TOC Variations in the Southern Red Sea: Monsoon Activity

[36] Although the relation is blurred to some extent by the complex pattern of the carbon isotopic record and the difference in resolution, visual examination reveals that, in general, TOC millennial-scale fluctuations during the glacial period are inversely correlated with *G. ruber* $\delta^{13}C$ changes (Figure 5). In other words, changes in surface water isotopic carbon composition do not primarily reflect variations in the preferential uptake of light ^{12}C carbon. Such a causal relationship would result in an increase (decrease) of *G. ruber* $\delta^{13}C$ associated with episodes of high (low) TOC, opposite to what we observe. Our data suggest, therefore, that at millennial-scale, *G. ruber* $\delta^{13}C$ mainly reflect the nutrient content of surface water masses advected above the site of core MD92-1008; primary productivity being enhanced (higher TOC) when surface waters have a low $\delta^{13}C$ signature. Further studies are in progress in order to decipher whether stratification and vertical redistribution of nutrients may have changed significantly at site MD92-1008 along our 60 ka record at this millennial scale. At this stage, as indicated above, we assume that stratification has always restrained vertical mixing in the Southern Red Sea. Thus, we suggest that the positive correlation between $CaCO_3$ and TOC and the inverse correlation between TOC and planktonic carbon isotope at the millennial-scale mainly reflect changes in primary productivity driven by the lateral advection of nutrient-rich surface waters to the site of core MD92-1008.

[37] Today, the flux and nutrient content of surface water masses entering the Red Sea through the Bab-el-Mandeb Strait are seasonally modulated by monsoon atmospheric circulation, with the summer monsoon winds promoting lateral advection into the Red Sea of nutrient-rich waters that are upwelled in the Gulf of Aden [*Jones and Browning*, 1971; *Murray and Johns*, 1997; *Naqvi et al*., 1986; *Poisson et al*., 1984; *Smeed*, 1997]. This advection of nutrient-rich waters boosts the primary productivity [*Weikert*, 1987]. By analogy, we suggest that millennial-scale oscillations in the TOC and $\delta^{13}C$ reflect changes in the intensity of the summer monsoon atmospheric circulation, which ultimately controlled the amplitude of Ekman pumping and, therefore, the nutrient content of waters that were laterally advected to the Red Sea across the Bab-el-Mandeb Strait. Today, nutrient advection mainly takes place at intermediate depths, during the summer monsoon [*Naqvi et al*., 1986; *Siddall et al*., 2004; *Smeed*, 1997; *Sofianos et al*., 2002]. Because of the lowered sea level and reduced sill depth at the Bab-el-Mandeb Strait during glacial periods, the nutrients could not have penetrated at intermediate depth waters and must have been advected in the thin layer of surface waters that entered the Red Sea. This lateral transfer may have been maximal during the winter monsoon (when wind forcing enhances transport of surface waters to the Red Sea), but we believe that the key aspect remains the intensity of summer monsoon winds which ultimately controlled the vertical nutrient recycling to the surface waters in the Gulf of Aden and the western Arabian Sea.

[38] Within the limits of our age model, the comparison of the high-resolution susceptibility record with the NGRIP $\delta^{18}O$ data set (Figure 5) clearly suggests that high productivity (higher TOC values, lower K values) was characteristic of interstadials, suggesting increased summer wind intensity and enhanced Ekman pumping at these periods. It is important to note that at the glacial-interglacial timescale, both $\delta^{13}C$ and TOC increased from the Last Glacial Maximum (LGM) to the Holocene and the anticorrelation between TOC and $\delta^{13}C$ that we observed at the millennial scale no longer holds. It is likely that regional effects are masked by global changes in nutrient inventory. About ~0.3‰ of ^{13}C increase across the last termination is readily explained, for instance, by the global transfer of carbon between the marine and continental realms [e.g., *Shackleton*, 1977].

5.5. Sedimentation in the Southern Red Sea During the Last Deglaciation

[39] After the LGM, during the deglaciation, all indicators exhibit large variations. In order to provide a clearer picture of these successive events, we have enlarged the 5–20 ka B. P. interval in Figure 6 and added the $\delta^{18}O$ curve (Figure 6) of the present core. Below, we summarize and interpret the successive major events that are derived from this set of records.

[40] 1. The onset of MIS 2 is characterized by an increase in K and RAMO, but low S ratios indicate that magnetic mineralogy was dominated by a large amount of high coercivity material, likely goethite. Because of low TOC contents, magnetite was not affected by dissolution. During this period, the sea level reached −120 m and exchanges between the Red Sea and the Gulf of Aden were channeled through a 6 km wide passage with a water depth that did not exceed 17 m [*Siddall et al*., 2003]. Our data show that productivity was weak (low TOC and low $CaCO_3$). We suggest that the large amount of goethite (coherent with high RAMO values) likely reflects an increased eolian transport (e.g., increased aridity). Alternatively, this late glacial increase in goethite could result from an enhanced erosion of exposed continental margins associated to sea level lowering; but we think that this second hypothesis is less likely owing to the arid environment around the Red Sea, which limits erosion. As we will see below, our data actually suggest that eolian material had been probably accumulating on the exposed margins during the glacial period and were remobilized rapidly during the rise of sea level.

[41] 2. The transition with the next episode is characterized by three large peaks in Th/Ta, K, and RAMO (Figure 6). The low S ratio indicates that goethite is the prominent magnetic carrier while the abundance of Th is likely indicative of volcanic material. The Th/Ta ratio differs from the rest of the record and indicates that this short episode was associated with a change of source. We do not disconnect these large changes from those linked to the sea level rise. We speculate that such strong peaks were caused by flushing of volcanic windborne material from the emerged sea margins following the onset of sea level rise. In this area, goethite and hematite are considered as eolian transported particles [*deMenocal*, 2004; *Jung et al*., 2004; *Kolla et al*., 1976; *Sirocko and Lange*, 1991; *Sirocko et al*., 2000; *van Campo et al*., 1982].

During sea level rise, the fraction of windborne detrital material deposited upon the previously exposed continental margins could be efficiently remobilized, particularly in the Bab-el-Mandeb area due to the active circulation associated to the channeled water fluxes ("flush effect").

[42] 3. Within the uncertainties inherent to our depth-age model (including potential changes in past reservoirs associated with the modulation of water exchanges and residence time), the ages of the next significant episode coincide with the Bølling-Allerød period (12.7–14.5 ka B.P.) [*McManus et al*., 2004] that has been documented at high latitudes. The magnetic parameters show a succession of oscillations in phase with $\delta^{18}O$. The positive correlation between the S ratio and K indicates that changes in magnetic concentration were driven by an enhanced concentration of magnetite (Figure 6). The $\delta^{13}C$ and the TOC fluctuations are opposite to each other, which may reflect the prominent role of advected nutrient-rich water in driving the surface carbon isotopic signature.

[43] 4. The next episode corresponds to the Younger Dryas (YD), as suggested by the structure of our planktonic $\delta^{18}O$ record. However, it is important to notice that the lower and upper limits of this episode in core MD92-1008 are a little older (13.7 ka B.P. and 11.7 ka B.P., respectively) than in the Atlantic records (i.e., extension from ~12.7 to 11 ka B.P.) [*McManus et al*., 2004; *Waelbroeck et al*., 2001]. Abrupt increases in TOC, S ratio and carbonate contents characterize this YD interval. Both K and RAMO progressively decrease and low levels of RAMO are associated with low K. The amount of organic matter (TOC) increases (while K decreases) in parallel with sea level. During this interval, the TOC still controls the evolution of magnetic mineralogy and magnetite is the preeminent magnetic oxide.

[44] An abrupt and puzzling episode of low $\delta^{13}C$ takes place at the beginning of this interval with isotopic values reaching the lowest level (−0.33‰) of the entire record and being associated with very high levels of TOC (~5%). This brief episode suggests the advection of waters particularly enriched in nutrients. It is not clear whether it can be linked to lateral advection through the Bab-el-Mandeb Strait, with a particularly strong contribution of intermediate water upwelled in the Gulf of Aden. Such low $\delta^{13}C$ values could also point out a rapid episode of vertical mixing, during which deeper waters from the Red Sea were forced toward the surface as water exchanges through the Bab-el-Mandeb Strait intensified. Further studies, including benthic foraminifera $\delta^{13}C$ data from this area, will hopefully clarify the mechanisms leading to this episode. The end of the Younger Dryas corresponds to a stabilization of all magnetic and geochemical parameters, which persists within the next period.

6. Conclusion

[45] We performed a multiproxy study of core MD92-1008 in order to decipher the impact of climate variability and water exchanges through the Bab-el-Mandeb Strait on sedimentation in the southernmost part of the Red Sea during the last 60 ka. A strong anticorrelation between TOC and changes in magnetic concentration reveal that reductive dissolution of magnetite during diagenesis has played a key role on the evolution of the magnetic concentration parameters. Although further work is in progress to address the origin of the TOC fluctuations and the importance of preservation, the aridity of the surrounding area and the strong correlation with changes in calcium carbonate suggest that the organic carbon was mostly of marine origin. Today, the Red Sea is a nutrient-depleted marginal sea and its productivity is dependent upon the lateral advection of nutrient-rich waters from the Gulf of Aden across the Bab-el-Mandeb Strait. At glacial-interglacial timescales, the strong resemblance between TOC and K records, in the one hand, and glacio-eustatic sea level changes, on the other hand, suggests that primary productivity may have been modulated by the amount of water exchanged through the Bab-el-Mandeb Strait. The deglaciation period reveals a complex history with high-amplitude swings recorded by several parameters. In particular, the rise in sea level was associated with a rapid flush of detrital material that was accumulated on the continental margins in the previously emerged zones of the Bab-el-Mandeb area.

[46] At the millennial scale, during MIS 3, the TOC variations may indicate past changes in productivity. The fact that high (low) TOC values are associated with low (high) planktonic $\delta^{13}C$ suggests that the carbon isotopic composition reflects changes in the nutrient content of advected waters. Today, nutrient-rich intermediate waters are upwelled in the Gulf of Aden during the summer monsoon and are laterally advected to the Red Sea through the Bab-el-Mandeb Strait. By analogy, we speculate that the millennial-scale variations of the TOC in the southernmost part of the Red Sea during MIS 3 reflect past changes in the intensity of summer monsoon winds and advection of nutrient-rich waters to the Red Sea, with increased (decreased) monsoon intensity during interstadial (stadial) episodes. However, due to the reduced sill depth at the Bab-el-Mandeb Strait, this lateral advection had to take place at the surface, whereas today, it mostly takes place at intermediate depths during the summer season.

[47] **Acknowledgments.** We are grateful to Pierre-Jean Giannesini for his help during sampling campaigns at the MNHN (Paris) and to François Baudin (ISTeP, UPMC, Paris) for providing the TOC measurements. We thank France Lagroix, Nicolas Thouveny, and Christophe Colin for stimulating discussions. This work was supported by the MAG-ORB program (ANR-09-BLAN-0053-01) from the French Agence Nationale de la Recherche. This is IPGP contribution 3431 and LSCE contribution 5033.

References

Abrajevitch, A., and K. Kodama (2011), Diagenetic sensitivity of paleoenvironmental proxies: A rock magnetic study of Australian continental margin sediments, *Geochem. Geophys. Geosyst.*, *12*, Q05Z24, doi:10.1029/2010GC003481.

Andersen, K. K., A. Svensson, S. J. Johnsen, S. O. Rasmussen, M. Bigler, R. Röthlisberger, and H. B. Clausen (2006), The Greenland ice core chronology 2005, 15–42 ka. Part 1: Constructing the time scale, *Quat. Sci. Rev.*, *25*, 3246–3257, doi:10.1016/j.quascirev.2006.08.002.

Arz, H. W., J. Pätzold, P. J. Müller, and M. O. Moammar (2003a), Influence of Northern Hemisphere climate and global sea level rise on the restricted Red Sea marine environment during termination I, *Paleoceanography*, *18*(2), 1053, doi:10.1029/2002PA000864.

Arz, H. W., F. Lamy, J. Pätzold, P. J. Müller, and M. Prins (2003b), Mediterranean moisture source for an early-Holocene humid period in the Northern Red Sea, *Science*, *300*, 118–121, doi:10.1126/science.1080325.

Arz, H. W., F. Lamy, and J. Pätzold (2006), A pronounced dry event recorded around 4.2 ka in brine sediments from the Northern Red Sea, *Quat. Res.*, *66*, 432–441, doi:10.1016/j.yqres.2006.05.006.

Arz, H. W., F. Lamy, A. Ganopolski, N. Nowaczyk, and J. Pätzold (2007), Dominant Northern Hemisphere climate control over millennial-scale glacial sea-level variability, *Quat. Sci. Rev.*, *26*, 312–321, doi:10.1016/j.quascirev.2006.07.016.

Aubourg, C., and J. P. Pozzi (2010), Toward a new < 250 ° C pyrrhotite–magnetite geothermometer for claystones, *Earth Planet. Sci. Lett.*, *294*, 47–57, doi:10.1016/j.epsl.2010.02.045.

Bassinot, F. C., C. Marzin, P. Braconnot, O. Marti, E. Mathien-Blard, F. Lombard, and L. Bopp (2011), Holocene evolution of summer winds and marine productivity in the tropical Indian Ocean in response to insolation forcing: Data-model comparison, *Clim. Past*, *7*, 815–829, doi:10.5194/cp-7-815-2011.

Biton, E., H. Gildor, and W. R. Peltier (2008), Red Sea during the Last Glacial Maximum: Implications for sea level reconstruction, *Paleoceanography*, *23*, PA1214, doi:10.1029/2007PA001431.

Bloemendal, J., J. W. King, F. R. Hall, and S.-J. Doh (1992), Rock magnetism of late Neogene and Pleistocene deep-sea sediments: Relationship to sediment source, diagenetic processes and sediment lithology, *J. Geophys. Res.*, *97*, 4361–4375, doi:10.1029/91JB03068.

Bouilloux, A., J.-P. Valet, F. Bassinot, J.-L. Joron, M.-M. Blanc-Valleron, E. Moreno, F. Dewilde, M. Kars, and F. Lagroix (2013), Diagenetic modulation of the magnetic properties in sediments from the Northern Indian Ocean, *Geochem. Geophys. Geosyst.*, *14*, 3779–3800, doi:10.1002/ggge.20234.

Burns, S. J., A. Matter, N. Frank, and A. Mangini (1998), Speleothem-based paleoclimate record from northern Oman, *Geology*, *26*, 499–502, doi:10.1130/0091-7613(1998)026<0499:SBPRFN>2.3.CO;2.

Caley, T., B. Malaizé, S. Zaragosi, L. Rossignol, J. Bourget, F. Eynaud, P. Martinez, J. Giraudeau, and N. Ellouz-Zimmermann (2011), New Arabian Sea records help decipher orbital timing of Indo-Asian monsoon, *Earth Planet. Sci. Lett.*, *308*, 433–444, doi:10.1016/j.epsl.2011.06.019.

Clemens, S. C., and W. L. Prell (1990), Late Pleistocene variability of Arabian summer monsoon winds and continental aridity: Eolian records from the lithogenic component of deep-sea sediments, *Paleoceanography*, *5*, 109–145, doi:10.1029/PA005i002p00109.

Clemens, S. C., D. W. Murray, and W. L. Prell (1996), Nonstationary phase of the pliopleistocene Asian monsoon, *Science*, *274*, 943–948.

Cogné, J. P. (2003), PaleoMac: A Macintosh™ application for treating paleomagnetic data and making plate reconstructions, *Geochem. Geophys. Geosyst.*, *4*(1), 1007, doi:10.1029/2001GC000227.

Coplen, T. B. (1988), Normalization of oxygen and hydrogen isotope data, *Chem. Geol.*, *72*, 293–297, doi:10.1016/0168-9622(88)90042-5.

DeMenocal, P. B. (2004), African climate change and faunal evolution during the Pliocene–Pleistocene, *Earth Planet. Sci. Lett.*, *220*, 3–24, doi:10.1016/S0012-821X(04)00003-2.

Emiliani, C. (1955), Pleistocene temperatures, *J. Geol.*, *63*, 538–578.

Fenton, M., S. Geiselhart, E. J. Rohling, and C. Hemleben (2000), Aplanktonic zones in the Red Sea, *Mar. Micropaleontol.*, *40*, 277–294, doi:10.1016/S0377-8398(00)00042-6.

Franke, C., T. Frederichs, and M. J. Dekkers (2007), Efficiency of heavy liquid separation to concentration magnetic particles, *Geophys. J. Int.*, *170*, 1053–1066, doi:10.1111/j.1365-246X.2007.03489.x.

Froelich, P. N., G. P. Klinkhammer, M. L. Bender, N. A. Luedtke, G. R. Heath, D. Cullen, P. Dauphin, D. Hammond, B. Hartman, and V. Maynard (1979), Early oxidation of organic matter in pelagic sediments of the eastern equatorial Atlantic: Suboxic diagenesis, *Geochim. Cosmochim. Acta*, *43*, 1075–1090, doi:10.1016/0016-7037(79)90095-4.

Grasshoff, K. (1975), The hydrochemistry of landlocked basins and fjords, in *Chemical Oceanography*, vol. 2, edited by J. P. Riley and J. Skirrow, pp. 456–597, Academic Press, New York.

Hemleben, C., D. Meischner, R. Zahn, A. Almogi-Labin, H. Erlenkeuser, and B. Hiller (1996), Three hundred eighty thousand year long stable isotope and faunal records from the Red Sea: Influence of global sea level change on hydrography, *Paleoceanography*, *11*, 147–156, doi:10.1029/95PA03838.

Jones, E. N., and D. G. Browning (1971), Cold water layer in the Southern Red Sea, *Limnol. Oceanogr.*, *16*, 503–509, doi:10.4319/lo.1971.16.3.0503.

Joron, J. L., M. Treuil, and L. Raimbault (1997), Activation analysis as a geochemical tool: Statement of its capabilities for geochemical trace element studies, *J. Radioanal. Nucl. Chem.*, *216*, 229–235, doi:10.1007/BF02033783.

Jung, S. J. A., G. R. Davies, G. M. Ganssen, and D. Kroon (2004), Stepwise Holocene aridification in NE Africa deduced from dust-borne radiogenic isotope records, *Earth Planet. Sci. Lett.*, *221*, 27–37, doi:10.1016/S0012-821X(04)00095-0.

Karlin, R., and S. Levi (1983), Diagenesis of magnetic minerals in Recent haemipelagic sediments, *Nature*, *303*, 327–330, doi:10.1038/303327a0.

Kawamura, N., H. Oda, K. Ikehara, T. Yamazaki, K. Shioi, S. Taga, S. Hatakeyama, and M. Torii (2007), Diagenetic effect on magnetic properties of marine core sediments from the southern Okhotsk Sea, *Earth Planets Space*, *59*, 83–93.

Kolla, V., L. Henderson, and P. Biscaye (1976), Clay mineralogy and sedimentation in the Western Indian Ocean, *Deep Sea Res.*, *23*, 949–961, doi:10.1016/0011-7471(76)90825-1.

Legge, H. L., J. Mutterlose, and H. W. Arz (2006), Climatic changes in the Northern Red Sea during the last 22,000 years as recorded by calcareous nannofossils, *Paleoceanography*, *21*, PA1003, doi:10.1029/2005PA001142.

Legge, H. L., J. Mutterlose, H. W. Arz, and J. Pätzold (2008), Nannoplankton successions in the Northern Red Sea during the last glaciation (60 to 14.5 ka B.P.): Reactions to climate change, *Earth Planet. Sci. Lett.*, *270*, 271–279, doi:10.1016/j.epsl.2008.03.030.

Leslie, B. W., D. E. Hammond, W. M. Berelson, and S. P. Lund (1990), Diagenesis in anoxic sediments from the California Continental Borderland and its influence on iron, sulfur, and magnetite behavior, *J. Geophys. Res.*, *95*, 4453–4470, doi:10.1029/JB095iB04p04453.

Leuschner, D. C., and F. Sirocko (2000), The low-latitude monsoon climate Dansgaard-Oeschger cycles and Heinrich Events, *Quat. Sci. Rev.*, *19*, 243–254, doi:10.1016/S0277-3791(99)00064-5.

Lévy, M., D. Shankar, J.-M. André, S. S. C. Shenoi, F. Durand, and C. de Boyer Montégut (2007), Basin-wide seasonal evolution of the Indian Ocean's phytoplankton blooms, *J. Geophys. Res.*, *112*, C12014, doi:10.1029/2007JC004090.

Lisiecki, L. E., and M. E. Raymo (2005), A Pliocene-Pleistocene stack of 57 globally distributed benthic delta O-18 records, *Paleoceanography*, *20*, PA1003, doi:10.1029/2004PA001071.

Liu, J., R. Zhu, A. P. Roberts, S. Li, and J.-H. Chang (2004), High-resolution analysis of early diagenetic effects on magnetic minerals in post-middle-Holocene continental shelf sediments from the Korea Strait, *J. Geophys. Res.*, *109*, B03103, doi:10.1029/2003JB002813.

Maher, B. A., V. V. Karloukovski, and T. J. Mutch (2004), High-field remanence properties of synthetic and natural submicrometre haematites and goethites: Significance for environmental contexts, *Earth Planet. Sci. Lett.*, *226*, 491–505, doi:10.1016/j.epsl.2004.05.042.

Malaizé, B., M. T. Vénec-Peyré, C. Joly, F. Bassinot, N. Caillon, and K. Charlier (2009), Imprints of high-salinity water plumes originating from the Red Sea during termination II, *Palaeogeogr. Palaeoclimatol. Palaeoecol.*, *276*, 69–79, doi:10.1016/j.palaeo.2009.02.027.

Martinson, D. G., N. G. Pisias, J. D. Hays, J. Imbrie, T. C. Moore Jr., and N. J. Shackleton (1987), Age dating and the orbital theory of the ice ages: Development of a high-resolution 0 to 300,000-year chronostratigraphy, *Quat. Res.*, *27*, 1–29, doi:10.1016/0033-5894(87)90046-9.

McManus, J. F., R. Francois, J. M. Gherardi, L. D. Keigwin, and S. Brown-Leger (2004), Collapse and rapid resumption of Atlantic meridional circulation linked to deglacial climate changes, *Nature*, *428*, 834–837, doi:10.1038/nature02494.

Meynadier, L., J.-P. Valet, R. Weeks, N. J. Shackleton, and V. Lee Hagee (1992), Relative geomagnetic intensity of the field during the last 140 ka, *Earth Planet. Sci. Lett.*, *114*, 39–57, doi:10.1016/0012-821X(92)90150-T.

Meynadier, L., J.-P. Valet, and F. E. Grousset (1995), Magnetic properties and origin of upper Quaternary sediments in the Somali Basin, Indian Ocean, *Paleoceanography*, *10*, 459–472, doi:10.1029/94PA03151.

Morcos, S. A. (1970), Physical and chemical oceanography of the Red Sea, *Oceanogr. Mar. Biol. Annu. Rev.*, *8*, 73–202.

Murray, S. P., and W. Johns (1997), Direct observations of seasonal exchange through the Bab el Mandab Strait, *Geophys. Res. Lett.*, *24*, 2557–2560, doi:10.1029/97GL02741.

Nagy, E. A., and J. Valet (1993), New advances for paleomagnetic studies of sediment cores using U-Channels, *Geophys. Res. Lett.*, *20*, 671–674, doi:10.1029/93GL00213.

Naqvi, S. W. A., H. P. Hansen, and T. W. Kureishy (1986), Nutrient uptake and regeneration ratios in the Red Sea with reference to the nutrient budgets, *Oceanol. Acta*, *9*, 271–275.

Neumann, A. C., and D. A. McGill (1962), Circulation of the Red Sea in the early summer, *Deep Sea Res.*, *8*, 223–235, doi:10.1016/0146-6313(61)90023-5.

North Greenland Ice Core Project members (2004), High-resolution record of Northern Hemisphere climate extending into the last interglacial period, *Nature*, *431*, 147–151, doi:10.1038/nature02805.

O'Reilly, W. (1984), *Rock and Mineral Magnetism*, 230 pp., Blackie, Glasgow.

Paillard, D., L. Labeyrie, and P. Yiou (1996), Macintosh program performs time-series analysis, *Eos Trans. AGU*, *77*, 379, doi:10.1029/96EO00259.

Pedgley, D. E. (1974), An outline of the weather and climate of the Red Sea, in *L'Oceanographie Physique de la Mer Rouge*, pp. 9–27 , CNEXO, Saclay, France.

Poisson, A., S. Morcos, E. Souvermezoglou, A. Papaud, and A. Ivanoff (1984), Some aspects of biogeochemical cycles in the Red Sea with special reference to new observations made in summer 1982, *Deep Sea Res.*, *31*, 707–718.

Prell, W. L., W. H. Hutson, D. F. Williams, A. W. Bé, K. Geitzrenauer, and B. Molfino (1980), Surface circulation of the Indian Ocean during the Last

Glacial Maximum, approximately 18,000 yr B.P, *Quat. Res.*, *14*, 309–336, doi:10.1016/0033-5894(80)90014-9.

Reimer, P. J., et al. (2009), IntCal09 and Marine09 radiocarbon age calibration curves, 0–50,000 years cal BP, *Radiocarbon*, *51*, 1111–1150.

Richter, C., A. Hayashida, Y. Guyodo, and K. L. Verosub (1999), Magnetic intensity loss and core diagenesis in long-core samples from the East Cortez Basin and the San Nicholas Basin (California Borderland), *Earth Planets Space*, *51*, 329–336.

Roberts, A. P., and G. M. Turner (1993), Diagenetic formation of ferrimagnetic iron sulphide minerals in rapidly deposited marine sediments, South Island, New Zealand, *Earth Planet. Sci. Lett.*, *115*, 257–273, doi:10.1016/0012-821X(93)90226-Y.

Robinson, S. G., J. T. S. Sahota, and F. Oldfield (2000), Early diagenesis in North Atlantic abyssal plain sediments characterized by rock-magnetic and geochemical indices, *Mar. Geol.*, *163*, 77–107, doi:10.1016/S0025-3227(99)00108-5.

Rohling, E. J., and W. J. Zachariasse (1996), Red Sea outflow during the Last Glacial Maximum, *Quat. Int.*, *31*, 77–83, doi:10.1016/1040-6182(95)00023-C.

Rohling, E. J., M. Fenton, F. J. Jorissen, P. Bertrand, G. Ganssen, and J. P. Caulet (1998), Magnitudes of sea-level lowstands of the past 500,000 years, *Nature*, *394*, 162–165, doi:10.1038/28134.

Rohling, E. J., K. Grant, C. Hemleben, M. Siddall, B. A. A. Hoogakker, M. Bolshaw, and M. Kucera (2007), High rates of sea-level rise during the last interglacial period, *Nat. Geosci.*, *1*, 38–42, doi:10.1038/ngeo.2007.28.

Rowan, C. J., A. P. Roberts, and T. Broadbent (2009), Reductive diagenesis, magnetite dissolution, greigite growth and paleomagnetic smoothing in marine sediments: A new view, *Earth Planet. Sci. Lett.*, *277*, 223–235, doi:10.1016/j.epsl.2008.10.016.

Shackleton, N. J. (1977), Carbon-13 in Uvigerina: Tropical rainforest history and the equatorial Pacific dissolution cycles, in *The Fate of Fossil Fuel CO2 in the Oceans*, edited by N. R. Andersen and A. Malahoff, pp. 401–427, Plenum Press, New York.

Sharma, G. S. (1978), Upwelling off the southwest coast of India, *Indian J. Mar. Sci.*, *7*, 209–218.

Sheppard C. R. C. (2000), The Red Sea, in *Seas at the Millennium—An Environmental Evaluation*, vol. 2, edited by C.R.C. Sheppard, pp. 35–45, Elsevier Science Inc., Pergamon, Amsterdam.

Shetye, S. R., A. D. Gouveia, S. S. C. Shenoi, D. Sundar, G. S. Michael, A. M. Almeida, and K. Santanam (1990), Hydrography and circulation off the west coast of India during the southwest monsoon 1987, *J. Mar. Res.*, *48*, 359–378, doi:10.1357/002224090784988809.

Siddall, M., E. Rohling, A. Almogi-Labin, C. Hemleben, D. Meischner, I. Schmelzer, and D. A. Smeed (2003), Sea-level fluctuations during the last glacial cycle, *Nature*, *423*, 853–858, doi:10.1038/nature01690.

Siddall, M., D. A. Smeed, C. Hemleben, E. J. Rohling, I. Schmelzer, and W. R. Peltier (2004), Understanding the Red Sea response to sea level, *Earth Planet. Sci. Lett.*, *225*, 421–434, doi:10.1016/j.epsl.2004.06.008.

Siedler, G. (1969), General circulation of water masses in the Red Sea, in *Hot Brines and Recent Heavy Metal Deposits in the Red Sea*, 131–137.

Sirocko, F. (2003), Global change: Ups and downs in the Red Sea, *Nature*, *423*, 813–814, doi:10.1038/423813a.

Sirocko, F., and H. Lange (1991), Clay mineral accumulation rates in the Arabian Sea during the late Quaternary, *Mar. Geol.*, *97*, 105–119, doi:10.1016/0025-3227(91)90021-U.

Sirocko, F., M. Sarnthein, H. Erlenkeuser, H. Lange, M. Arnold, and J. C. Duplessy (1993), Century-scale events in monsoonal climate over the past 24,000 years, *Nature*, *364*, 322–324, doi:10.1038/364322a0.

Sirocko, F., D. Garbe-Schönberg, and C. Devey (2000), Processes controlling trace element geochemistry of Arabian Sea sediments during the last 25,000 years, *Global Planet. Change*, *26*, 217–303, doi:10.1016/S0921-8181(00)00046-1.

Smeed, D. (1997), Seasonal variation of the flow in the strait of Bab al Mandab, *Oceanol. Acta*, *20*, 773–781.

Snowball, I. F. (1993), Geochemical control of magnetite dissolution in subarctic lake sediments and the implications for environmental magnetism, *J. Quat. Sci.*, *8*, 339–346, doi:10.1002/jqs.3390080405.

Sofianos, S. S., W. Johns, and S. P. Murray (2002), Heat and freshwater budgets in the Red Sea from direct observations at Bab el Mandeb, *Deep Sea Res., Part II*, *49*, 1323–1340, doi:10.1016/S0967-0645(01)00164-3.

Southon, J., M. Kashgarian, M. Fontugne, B. Metivier, and W. W. S. Yim (2002), Marine reservoir corrections for the Indian Ocean and Southeast Asia, *Radiocarbon*, *44*, 167–180.

Stuiver, M., and P. J. Reimer (1993), Extended 14C data base and revised Calib 3.0 14C age calibration program, *Radiocarbon*, *35*, 215–230.

Trommer, G., M. Siccha, E. J. Rohling, K. Grant, M. T. J. van der Meer, S. Schouten, C. Hemleben, and M. Kucera (2010), Millennial-scale variability in Red Sea circulation in response to Holocene insolation forcing, *Paleoceanography*, *25*, PA3203, doi:10.1029/2009PA001826.

Van Campo, E., J. C. Duplessy, and M. Rossignol-Strick (1982), Climatic conditions deduced from a 150-kyr oxygen isotope-pollen record from the Arabian Sea, *Nature*, *296*, 56–59, doi:10.1038/296056a0.

Waelbroeck, C., J. C. Duplessy, E. Michel, L. Labeyrie, D. Paillard, and J. Duprat (2001), The timing of the last deglaciation in North Atlantic climate records, *Nature*, *412*, 724–727, doi:10.1038/35089060.

Waelbroeck, C., L. Labeyrie, E. Michel, J. C. Duplessy, J. McManus, K. Lambeck, E. Balbon, and M. Labracherie (2002), Sea-level and deep water temperature changes derived from benthic foraminifera isotopic records, *Quat. Sci. Rev.*, *21*, 295–305, doi:10.1016/S0277-3791(01)00101-9.

Weikert, H. (1987), Plankton and the pelagic environment, in *Red Sea*, Key Environments, vol. 7, edited by F. J. Edward and S. M. Head, pp. 90–111, Pergamon Press, Oxford.